A joint Monte Carlo analysis of seafloor compliance, Rayleigh wave dispersion and receiver functions at ocean bottom seismic stations offshore New Zealand

Justin S. Ball[1], Anne F. Sheehan[1], Joshua C. Stachnik[2], Fan-Chi Lin[3], and John A. Collins[4]

[1]CIRES and Department of Geological Sciences, University of Colorado at Boulder, Colorado, USA, [2]Department of Earth and Environmental Sciences, Lehigh University, Bethlehem, Pennsylvania, USA, [3]Department of Geology and Geophysics, University of Utah, Salt Lake City, Utah, USA, [4]Department of Geology and Geophysics, Woods Hole Oceanographic Institution, Woods Hole, Massachusetts, USA

Abstract Teleseismic body-wave imaging techniques such as receiver function analysis can be notoriously difficult to employ on ocean-bottom seismic data due largely to multiple reverberations within the water and low-velocity sediments. In lieu of suppressing this coherently scattered noise in ocean-bottom receiver functions, these site effects can be modeled in conjunction with shear velocity information from seafloor compliance and surface wave dispersion measurements to discern crustal structure. A novel technique to estimate 1-D crustal shear-velocity profiles from these data using Monte Carlo sampling is presented here. We find that seafloor compliance inversions and P-S conversions observed in the receiver functions provide complimentary constraints on sediment velocity and thickness. Incoherent noise in receiver functions from the MOANA ocean bottom seismic experiment limit the accuracy of the practical analysis at crustal scales, but synthetic recovery tests and comparison with independent unconstrained nonlinear optimization results affirm the utility of this technique in principle.

1. Introduction

The seafloor is a challenging environment for seismologists. Noise presents a significant obstacle to the ocean bottom seismometer (OBS) analyst. A diverse range of physical processes in the ocean and solid Earth generate seismoacoustic energy across a wide spectrum ranging from tidal periods to the microseism band and above [*Crawford et al.*, 1991; *Godin and Chapman*, 1999]. This "rich wavefield" [*Ritzwoller and Levshin*, 2002] recorded on seafloor seismometers can be either vexatious or auspicious to the investigator, depending on the task at hand.

Body-wave methods utilizing horizontal-component information such as shear-wave splitting and receiver functions are particularly difficult with OBS data. High-amplitude current-induced tilt noise is often observed on OBS horizontal channels [*Webb*, 1998], and a ubiquitous diffuse infragravity wavefield is recorded on all components at periods greater than about 40 s [*Crawford et al.*, 1991; *Webb*, 1998; *Willoughby and Edwards*, 2000]. Between 2 and 10 s period, microseismic noise prevails [*Webb*, 1998], and at infrasonic frequencies above 5 Hz hydroacoustic phases can be prevalent. Simple filtering is not always effective in improving OBS data quality due to this diverse noise spectrum.

At typical OBS sites, even high signal-to-noise ratio (SNR) events are distorted by reverberations in the water and shallow sediment columns that overprint deeper arrivals in the receiver function [*Leahy et al.*, 2010]. Large volumes of low shear-velocity marine sediments can also impose delays in teleseismic traveltimes that necessitate static corrections [*Harmon et al.*, 2007]. Mitigating these effects is a subject of active interest in the marine seismology community.

The seafloor noise wavefield can be utilized to elucidate velocity structure. Ambient Noise Tomography (ANT) of Rayleigh waves effectively resolves group and phase velocity dispersion at periods from 6 to 27 s, which can be inverted for shear-velocity structure [*Lin et al.*, 2007]. In similar fashion, the seafloor's response to loading by infragravity waves (the seafloor compliance) from 50 to 250 s also depends on the shear velocity structure beneath the OBS [*Crawford et al.*, 1991; *Willoughby and Edwards*, 2000]. Observed shear resonances in the sediment column excited by ambient noise can also constrain shallow sediment velocities [*Godin and Chapman*, 1999].
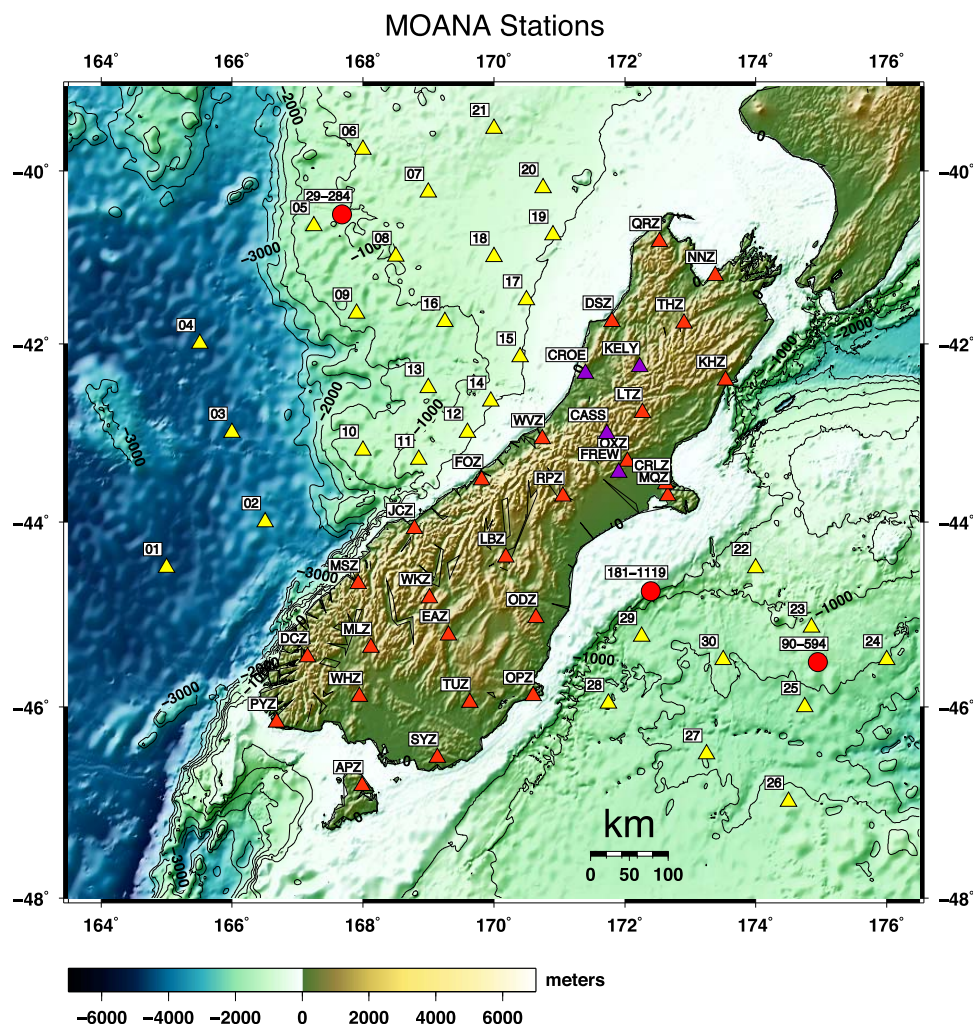
Figure 1. Map showing topography and bathymetry on and surrounding South Island of New Zealand. Yellow triangles represent ocean-bottom seismographs (OBS) deployed during the MOANA experiment. Purple triangles are land stations deployed during the same experiment. Red triangles are permanent GeoNet stations. OBS stations NZ16 and NZ06 are analyzed in this paper. Red circles show IODP boreholes used to ground-truth the analysis.

In this paper, we combine the shear velocity information obtained from the ambient noise observations (dispersion and compliance) with receiver functions in hopes of teasing out crustal arrivals obscured by sediment reverberations in the receiver functions, with application to OBS data from offshore New Zealand.

1.1. MOANA Experiment and Geologic Setting

The Marine Observations of Anisotropy Near Aotearoa (MOANA) experiment included the deployment of 30 broadband OBS and Differential Pressure Gauges (DPG) off both east and west coasts of the South Island of New Zealand from 2009 to 2010 (Figure 1) [*Yang et al.*, 2012]. The purpose of MOANA is to characterize the rheological controls on upper mantle deformation and its spatial extent in the region using observations of anisotropy as a strain gauge [*Zietlow et al.*, 2014; *Collins and Molnar*, 2014].

The MOANA stations off the South Island's East coast are situated in and around the inner Bounty Trough, a Cretaceous extensional basin containing thick deposits (up to 6 km) of terrigenous and marine sediments. Prior studies estimate crustal thicknesses of 18–25 km beneath the Eastern MOANA array and suggest the presence of a seismically fast, thin (~3 km) lower crustal layer [*Scherwath et al.*, 2003; *Van Avendonk et al.*, 2004] of possibly relict oceanic crust.

The Western MOANA array is mostly situated on the Challenger Plateau, an area of relatively undeformed submerged continental crust of the Australian plate estimated to range in thickness from 18 to 27 km
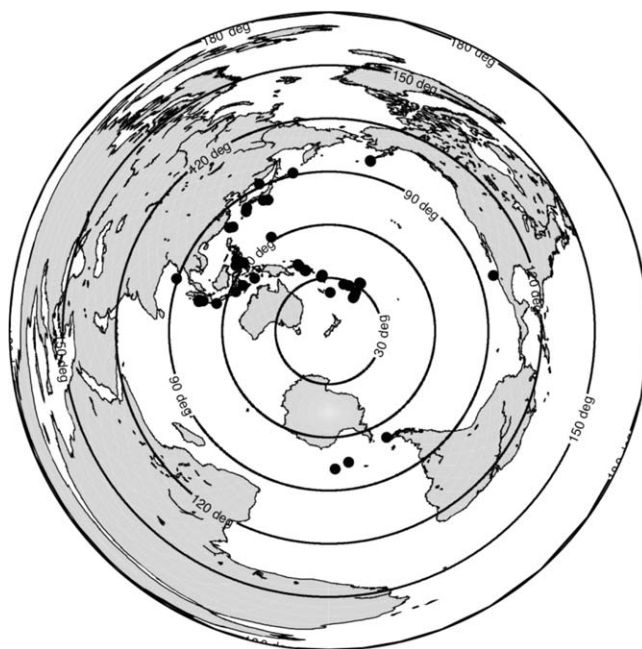
Figure 2. Distribution of earthquakes used in receiver function analysis. Analysis was restricted to earthquakes with magnitudes greater than 6.0 and epicentral distances of 20 100°. A total of 93 events were found to fit these criteria.

beneath the MOANA OBS sites [*Scherwath et al.*, 2003; *Van Avendonk et al.*, 2004; *Wood and Woodward*, 2002]. A layer of high-grade metamorphic rock in the lower crust beneath the plateau is postulated to be responsible for high lower-crustal velocities observed in active-source studies off the West coast [*Scherwath et al.*, 2003]. Sediment thicknesses beneath the Western array are estimated from sonobuoy and seismic reflection data to range from 460 to 800 m [*Divins*, 2003]. The gravity modeling of *Wood and Woodward* [2002] estimates sediment thicknesses to be 1–3 km in the same locations assuming constant densities in the sediment and basement of 2.33 and 2.78 g/cm^3, respectively.

In 1975, leg 29 of the Deep Sea Drilling Project (DSDP) took sediment core samples from site 284 on the Challenger Plateau at a distance of ~100 and ~160 km from stations NZ06 and NZ16, respectively. They recovered a 200 m section of homogeneous calcareous ooze lacking in detrital minerals and terrigenous sediments and dating to the late Miocene at depth. Sonic logs of the core yield a bulk average Vp of 1.57 ± 0.02 km/s. The core did not penetrate to basement rock and based on shipboard sub bottom profiler data sediment thickness was estimated to exceed 600 m [*Kennett et al.*, 1975].

2. Data

The analyses presented below reveal information about absolute subsurface S-velocities (via Rayleigh-wave dispersion, seafloor compliance) and the trade-off between bulk velocities and interface depths (via receiver functions). These data are forward-modeled over thousands of realizations of randomly perturbed model states via a Markov Chain Monte Carlo (MCMC) algorithm [*Haario et al.*, 2006] (section 3) to produce a suite of model realizations fitting the data to within a user-specified tolerance. In this section, we describe the data that go into our MCMC algorithm.

2.1. OBS Receiver Function Estimation

Teleseismic receiver functions are estimates of the near-receiver shear-wave impulse-response to an incident P-wave, and are obtained by deconvolving the radial component seismogram by the vertical component (a proxy for the source-time function) [e.g., *Langston*, 1979; *Owens et al.*, 1988]. We calculate receiver functions from the MOANA experiment OBS data using earthquakes of mb>6.0 and the epicentral distance range of 20–100° (Figure 2). A total of 93 events were found to fit these criteria, and low-SNR events were manually culled on a per-station basis. An extensive variety of frequency passbands were evaluated. In this study, we utilize a passband of 0.5–5 Hz for sedimentary layer analysis, and 0.05–2.5 Hz for deeper crustal and Moho analysis.

We use the multitaper spectral correlation algorithm of *Park and Levin* [2000] to produce the receiver function stacks employed in this analysis (Figure 3). This method produces coherence-weighted stacks in epicentral distance bins, suppressing random noise by stacking multiple receiver functions in the frequency domain. Since the majority of high-SNR teleseisms recorded by MOANA are clustered in epicentral distance ranges of ~30 and ~90°, only bin-averaged receiver functions from these distances were employed in this
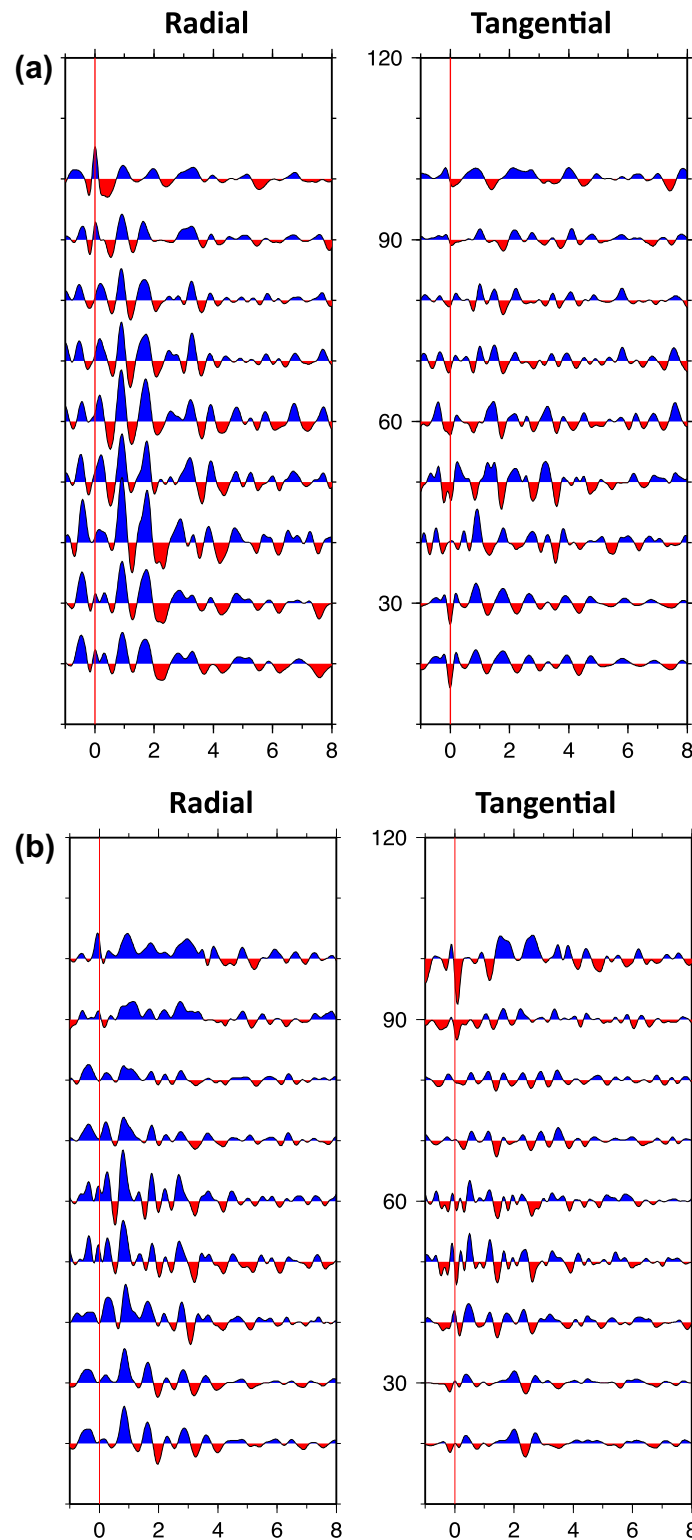
Figure 3. (a) Radial (left) and tangential (right) receiver function stacks for station NZ16, binned by epicentral distance and stacked with weight determined from vertical-horizontal coherence (see text for details). Azimuthal smoothing is applied via 10° overlap in epicentral bins. Positive arrivals are shown in blue, negative in red. The RF stack from the 30° bin was employed in this analysis because it contains the greatest number of high-SNR teleseisms. (b) Radial (left) and tangential (right) receiver function stacks for station NZ06. As in Figure 3a, the RF stack from the 30° bin was used due to the large number of high-SNR events it contains.

study. Average estimated slownesses corresponding to these distance ranges were incorporated into the forward modeling of receiver functions by the Monte Carlo algorithm.

2.1.1. Sediment Effects on OBS Receiver Functions

General features of receiver functions in marine sediments are common to those observed in sedimentary basins on land [*Hetényi et al.*, 2006; *Langston*, 2011; *Park and Levin*, 2000]. The dominant early mode-converted arrivals observed in MOANA receiver functions result from shallow impedance contrasts in the sediments (Figure 3). Very large shear velocity contrasts are possible across the sediment-basement contact [*Godin and Chapman*, 1999; *Harmon et al.*, 2007] giving rise to a strong pulse in the receiver functions at delay times of ∼1 s (depending on sediment thickness). These strong early pulses are the most coherent feature in MOANA receiver function waveforms across all epicentral distance bins (Figure 3). The free surface of the ocean is a near-perfect reflector for upgoing P waves in the water column, causing water multiples to be observed on OBS receiver functions [*Bostock and Trehu*, 2012]. Crustal multiples and unambiguous Moho-converted arrivals are not clearly observable in MOANA receiver functions.

We investigated the relative contributions of water and sediment multiples to receiver function amplitudes using synthetic seismograms [*Herrmann and Ammon*, 2004; *Herrmann*, 2013] (Figure 4). As model sediment thickness is increased, the sediment-basement P-S converted arrival is observed at later times, as expected. The interference behavior between sediment, water, and crustal reverberations is complex and highly sensitive to sediment properties. Figure 4 illustrates the subtle modulation of the dominantly sediment-controlled receiver function signal by the Moho-converted shear-wave arrival that we seek to resolve in this analysis. The red traces in Figure 4 are computed for a model with water and sediments over a crustal-velocity half-space, and the blue traces are for a model with water, sediments, and a crustal layer over a mantle half-space (i.e., blue trace is for a model with a Moho, red trace does not have a Moho). The difference between the two reflects the small magnitude of Moho P-S conversion and reverberations that we hope to resolve from beneath the sediment signal.

2.2. Absolute S-Velocity Estimation

Absolute shear velocity information is estimated from Rayleigh-wave dispersion and seafloor compliance and is used to better model the sediment reverberations in the receiver functions. Both surface wave dispersion and seafloor compliance are determined using recordings of ambient noise.

2.2.1. Rayleigh Dispersion

OBS sites are relatively quiet at periods in the "noise notch" from ∼10 to 30 s [*Crawford et al.*, 1991; *Webb*, 1998; *Willoughby and Edwards*, 2000], allowing robust seafloor Rayleigh dispersion curves to be estimated in this band [e.g., *Forsyth et al.*, 1998; *Ye et al.*, 2013]. Rayleigh waves at these periods are most sensitive to velocity structure from approximately 15–45 km depth. Group velocity dispersion from ambient noise tomography following the method of *Stachnik et al.* [2008] and phase velocity dispersion derived from earthquakes and ambient noise [*Lin et al.*, 2008, 2009] were determined using frequency-time analysis. The ambient noise tomography employed stacked one-bit normalized cross-correlations of hourly data windows between all station pairs. The resulting phase and group velocity maps were sampled at MOANA station locations to produce the dispersion curves presented here.

To estimate starting models in agreement with our Rayleigh dispersion data, we first performed a damped, linearized inversion of dispersion measurements from MOANA OBS stations. Group and phase velocity dispersion at each station was inverted for shear velocity models using the surf96 software from the CPS330 package of *Herrmann and Ammon* [2004]. This software performs a damped, linearized least-squares inversion for shear velocities in a stack of discrete layers.

The inversion was performed using a fixed-velocity water layer and a constant-velocity starting model ($Vs = 4.7$ km/s). The algorithm then solves for Vs in a stack of layers of increasing thickness from 1–10 km with depth, and the results are used to formulate starting models for the Monte Carlo analysis.

2.2.2. Seafloor Compliance

The nonlinear interaction of ocean surface gravity waves generates propagating infragravity-band (50–250 s) waves that attenuate very little on a basin-wide scale due to their long wavelengths (10–50 km) [*Webb*, 1998]. Infragravity waves excite evanescent displacements on the seafloor with depth sensitivity
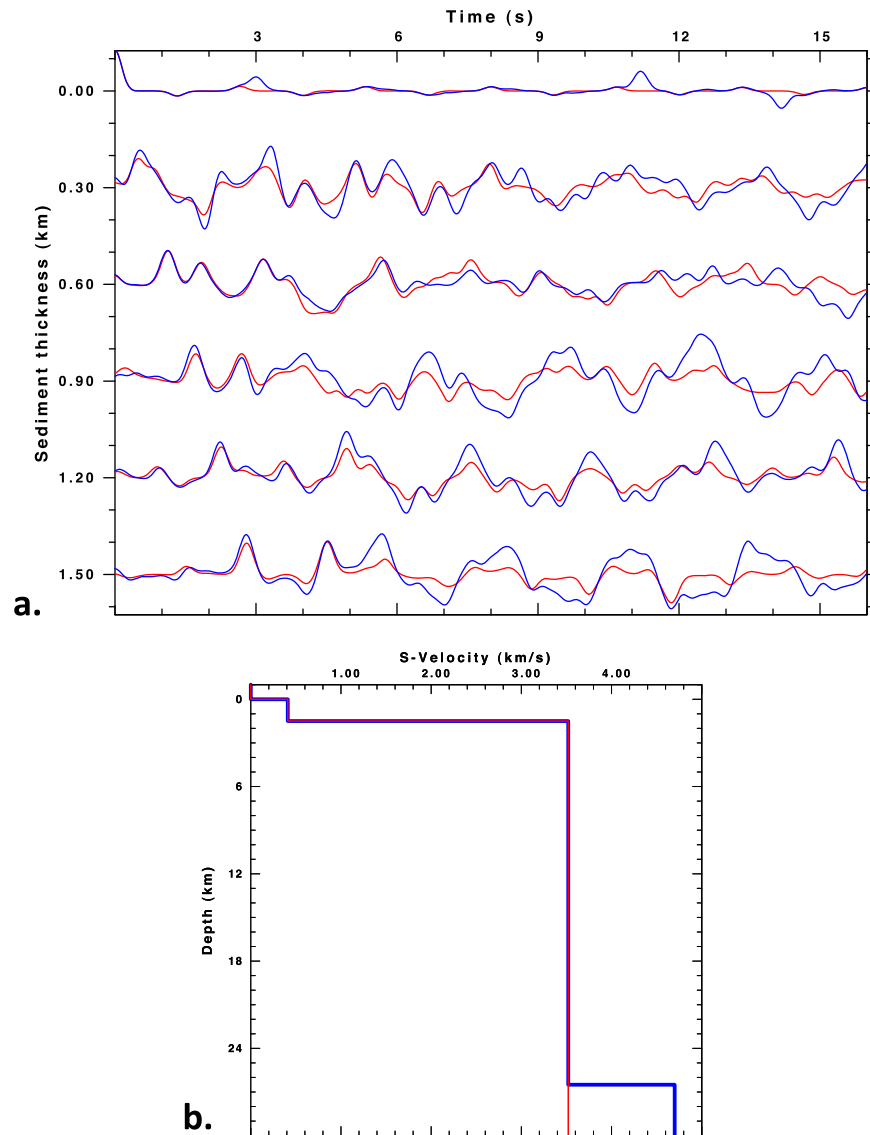
Figure 4. Synthetic receiver functions illustrating the effects of sediment and water layers on the RF waveform. (a) Blue traces are synthetic receiver functions generated from model with 1 km water, varying sediment thickness, and Moho at 25 km. (b). Red traces are synthetic receiver functions generated from model with 1 km water, varying sediment, and crustal half-space (no Moho). Sediment thickness varies from 0 km (top traces) to 1.5 km (bottom traces). Sediment Vs = 400 m/s. (bottom) Input velocity models for case with 1.5 km thick sediment. The difference between red and blue synthetic receiver functions illustrates the subtle modulating effect of the Moho P-S conversion on the sediment-dominated signal.

proportional to the forcing period and elastic parameters of the subsurface, for which we seek to solve [*Crawford et al.*, 1991; *Willoughby and Edwards*, 2000].

MOANA OBS instruments included a differential pressure gauge (DPG) with a relatively flat frequency response extending to infragravity periods. Pressure (from the DPG) and acceleration (from the vertical component of the broadband OBS seismometer) fields can be measured and their transfer function in the frequency domain yields the seafloor compliance [*Crawford et al.*, 1991; *Willoughby and Edwards*, 2000]:

$$\xi(\omega) = \frac{k(\omega)\gamma(\omega)}{\omega^2}\sqrt{\frac{S_a(\omega)}{S_p(\omega)}} \tag{1}$$

where $\xi(\omega)$ is seafloor compliance at angular frequency ω, k is wave number, S_a and S_p are acceleration and pressure power spectral densities (PSDs), and γ is the pressure-displacement coherence.
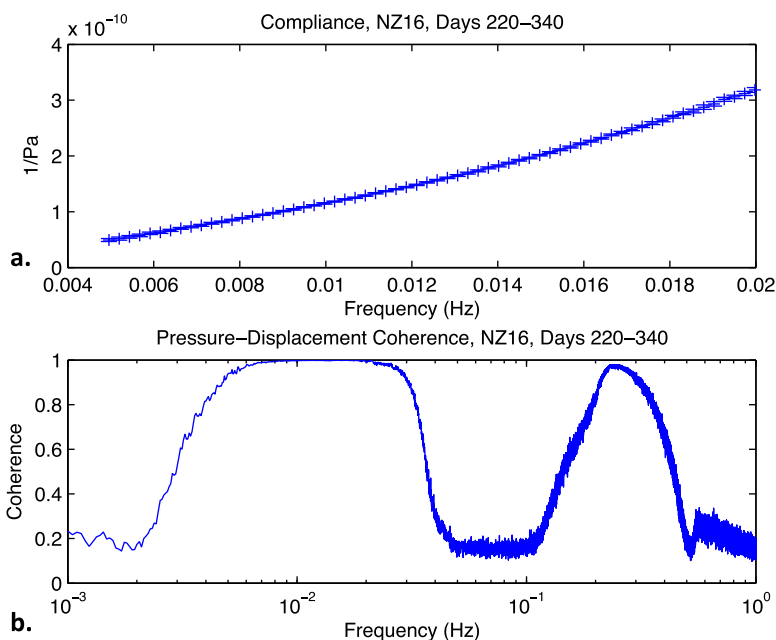
Figure 5. (a) Seafloor compliance spectrum obtained from 120 days of infragravity noise at station NZ16. Compliance uncertainty was estimated using equation (2). (b) Coherence between the pressure and vertical acceleration for the same 120 days at NZ16. Coherence is very high at NZ16 in the infragravity (0.004–0.02 Hz) and microseism (0.2–0.3 Hz) bands.

We estimated seafloor compliance for the MOANA stations using stacked multitaper power spectral densities computed for hour-long sliding windows over 24 h data segments encompassing 120 days of continuous data. Windows containing earthquakes or transients were rejected automatically based on their low pressure-vertical coherence.

Subsequently a gain correction obtained from the pressure-acceleration transfer functions of Rayleigh waves from five large earthquakes was applied to the compliance functions. At periods much longer than the quarter-wave resonance period of the water column, a Rayleigh wave at the seafloor exerts a force on a water column of depth H equal to its mass (ρH) times the seabed acceleration. Thus at periods around 30 s, we expect the transfer function between seafloor pressure P and acceleration A to be described by P/A$=\rho$H [*Filloux*, 1983] (S. C. Webb, personal communication, 2012). For 28 stations we investigated, the mean and standard deviation of the normalized transfer functions are 0.9 $\pm$ 0.1 *ρH. We found the transfer function for NZ16 to equal ρH within our measurement uncertainty and that for NZ06 to deviate from ρH by a factor of 0.7 $\pm$ 0.1. Thus to calibrate our compliance curve for NZ06, we divided it by 0.7, and we did not apply a correction to NZ16. This technique is particularly useful for seafloor compliance because since the pressure-acceleration transfer function is calibrated, errors in either the acceleration response or the DPG response are corrected simultaneously. Also, if the acceleration response is assumed to be correct, error in the nominal DPG gain factor can be estimated.

We estimate compliance uncertainty ε based on the pressure-displacement coherence γ following *Crawford et al.* [1991]:

$$\varepsilon[|\xi(\omega)|] = \frac{[1-\gamma^2(\omega)]^{1/2}}{|\gamma(\omega)|\sqrt{2n_d}}|\xi(\omega)| \tag{2}$$

where n_d is the number of data windows used to estimate the coherence and compliance functions.

We find compliance values ranging from approximately 10-9-10-10 Pa-1 at western MOANA sites (Figure 5), implying similar seafloor rigidities to those modeled at sites on calcareous sediments on the East Pacific Rise [*Willoughby and Edwards*, 2000]. *Crawford et al.* [1991] report similar compliance values for sites on hemipelagic sediments off California, and compliances as low as 3*10–11 Pa-1 are found for sediment-free oceanic crust off Cascadia.

3. Monte Carlo Inversion of Dispersion, Compliance, and Receiver Functions

We utilize a Markov Chain Monte Carlo (MCMC) algorithm to find shear velocity models that jointly fit the dispersion, compliance, and receiver functions. In contrast to many linearized inversion schemes, the MCMC method searches a broad model space and yields a suite of output models and their associated conditional probabilities rather than converging to a single "best-fitting" model [*Mosegaard and Tarantola*, 1995]. We adapted the Delayed-Rejection Adaptive Metropolis (DRAM) Monte Carlo algorithm from the MCMC Matlab Toolbox of *Haario et al.* [2006]. Our misfit functional and Gaussian model distributions were configured following *Shen et al.* [2013]. At each time step, a traditional MCMC algorithm randomly perturbs the starting model parameters and computes the joint misfit:

$$S_{JOINT}(m) = S_{SW} + \frac{1}{\kappa} S_{RF} + \frac{1}{\alpha} S_{SFC} \tag{3}$$

Where S_{SW}, S_{RF}, S_{SFC} are the least-squares misfits of surface wave, receiver function, and seafloor compliance data for model realization m. The least-squares misfit of each data set is scaled to the surface-wave data using ad hoc cost-function weighting parameters κ and α for the receiver functions and seafloor compliance, respectively. The relative cost function weights κ and α are chosen by inspection between inversion runs to weight the contribution of each dataset to the joint misfit approximately equally. The scaled misfit is then used to form a Gaussian likelihood functional:

$$L(m) = \exp\left(-\frac{1}{2} S(m)\right) \tag{4}$$

A trial model mi is accepted into the posterior distribution with a probability of 1 if its likelihood is greater than the current model mj. If this is not the case, a conditional probability is assigned to model mj based on [*Shen et al.*, 2013]:

$$P_{accept} = \begin{cases} 1, & L(m_i) \geq L(m_j) \\ \dfrac{L(m_i)}{L(m_j)} & L(m_i) < L(m_j) \end{cases} \tag{5}$$

The end result is a set of accepted model realizations with posterior model parameter variances that depend in this case on the choice of weighting parameters. If a full data covariance matrix were available, we could construct a joint likelihood function from the product of the likelihoods of the individual datasets and present meaningful model uncertainties within a Bayesian framework following *Shen et al.* [2013]. However, robust receiver function noise covariance estimates for MOANA data are difficult to determine using bootstrap or harmonic stripping techniques [*Shen et al.*, 2013] given the small number of usable receiver functions we employ compared to typical land-based studies.

The DRAM algorithm offers enhanced resistance to local minima over traditional Metropolis-Hastings implementations and reduces the necessity of accurate initial variance estimates [*Haario et al.*, 2006] which are specifically difficult to assess in our receiver function data given the paucity of useable events for bootstrap uncertainty analysis. Delayed rejection is a modification to the Metropolis-Hastings algorithm that allows additional local perturbation steps within each global time step if the likelihood has decreased at the current model state. To complement the benefits of delayed rejection, Adaptive Metropolis forces a global perturbation if the joint likelihood has failed to increase after a preset number of iterations (50–500 in this study), thus continually adapting the covariance of the proposal distribution. Together these modifications to the Metropolis-Hastings Monte Carlo estimator used by *Shen et al.* [2013] allow the analyst to optimize the trade-off between model-space size and chain mixing time while improving the chances of convergence to the global target distribution [*Haario et al.*, 2006]. To allow the Markov chains to evolve to a stable state before models are kept in the posterior distributions, a "burn-in" period of 500–10,000 iterations is first performed in which output model realizations are discarded.

The final posterior distributions are presented as histograms of model parameters, and the mean values of the Markov Chains represent the preferred velocity model parameters.

3.1. Model Parameterization

We evaluate two different parameterization schemes at sedimentary and crustal scales. In each case, the Monte Carlo algorithm searches a model space of six parameters that define either three constant-velocity

Table 1. Model Parameters Used for Synthetic Recovery Test

Layer	Thickness (km)	Vp (km/s)	Vs (km/s)	Density (kg/m^3)
Water	1	1.5	0	1
Calcareous Ooze	1	1.6	0.4	1.7
Limestone	1	3.6	1.9	2.5
Crust	24	6.5	3.6	2.7
Mantle	Half-space	8.1	4.7	3.3

layers or two sediment layers with linear velocity gradients and a discontinuity possible between them. In the linear-gradient parameterization, we solve for the shear velocity at the top and bottom of each sediment layer (vs1,vs2,vs3,vs4) and two layer thicknesses (h1,h2). The gradients are then discretized into constant-velocity layers of equal thickness.

In the constant-velocity parameterization, we solve for three velocities (vs1,vs2,vs3) and three thicknesses (h1,h2,h3).

To model Vp in the uppermost sediment layer, we use the average value measured at DSDP Site 284 of Vp $= 1.57 \pm 0.02$ km/s. The value in the Site 284 core log does not increase strongly with depth in the upper 200 m of sediments [*Kennett et al.*, 1975].

We use the "mudrock" equation of *Castegna et al.* [1985] to estimate Vp given Vs in the lower sediment layers:

$$Vp = 1.16^* \, Vs + 1.36 \; (km/s) \tag{6}$$

Densities in all sediment layers were modeled using the empirical relation from *Willoughby and Edwards* [2000]:

$$\rho(z) = 1.7 + (0.2/300) \; z \; (g/cc) \tag{7}$$

For the crustal scale inversion, we solve for a single sediment layer over a simple crustal model of two uniform layers atop a mantle half-space. The algorithm searches over thickness and Vs of each of these layers. This parameterization was adopted to avoid overfitting the data yet still potentially resolve such targets as hypothesized fast lower-crustal layers on both sides of the island [*Stern et al.*, 2002; *Van Avendonk et al.*, 2004], or consolidated basin sediments [*Wood and Woodward*, 2002]. A Vp/Vs ratio of 1.80 was assumed in the crust and mantle, and an uppermost mantle P-velocity of 8.1 km/s was assumed based on the results of the SIGHT experiment [*Stern et al.*, 2002; *Van Avendonk et al.*, 2004].

3.2. Solving the Forward Problems

Synthetic receiver functions were estimated using the program *hspec96p* from the CPS330 package of *Herrmann* [2013]. Rayleigh-wave phase-velocity and group-velocity dispersion was forward modeled using the *sdisp* routine of *Herrmann* [2013], and we use the 1-D forward modeling routine of *Crawford et al.* [1991] to calculate seafloor compliance. For each model realization synthetic receiver functions, Rayleigh-wave phase-velocity and group-velocity dispersion, and seafloor compliance are calculated and compared to the observed values.

4. Results

4.1. Synthetic Recovery Test

Synthetic recovery tests were performed using the same dispersion and compliance frequencies and receiver function estimation parameters employed on the real data. For a given starting Earth model (Table 1), synthetic surface wave dispersion, seafloor compliance, and receiver functions were generated. We added random Gaussian noise with standard deviations of 0.035 km/s and 7*10–12 Pa-1 to the synthetic phase-velocity dispersion and seafloor compliance data, respectively, values which are comparable to our actual measurement uncertainties. Real preevent noise waveforms were added to the synthetic vertical and radial components before deconvolution and scaled to produce synthetic receiver functions with SNR ranging from 1 to 10. The synthetic data were then used as input to the Monte Carlo analysis.

Results from 10,000 iterations using a naïve starting model are shown in Figure 6. We find that the MC method accurately and reliably recovers the "true" crustal model for receiver function SNR of 10 and above,
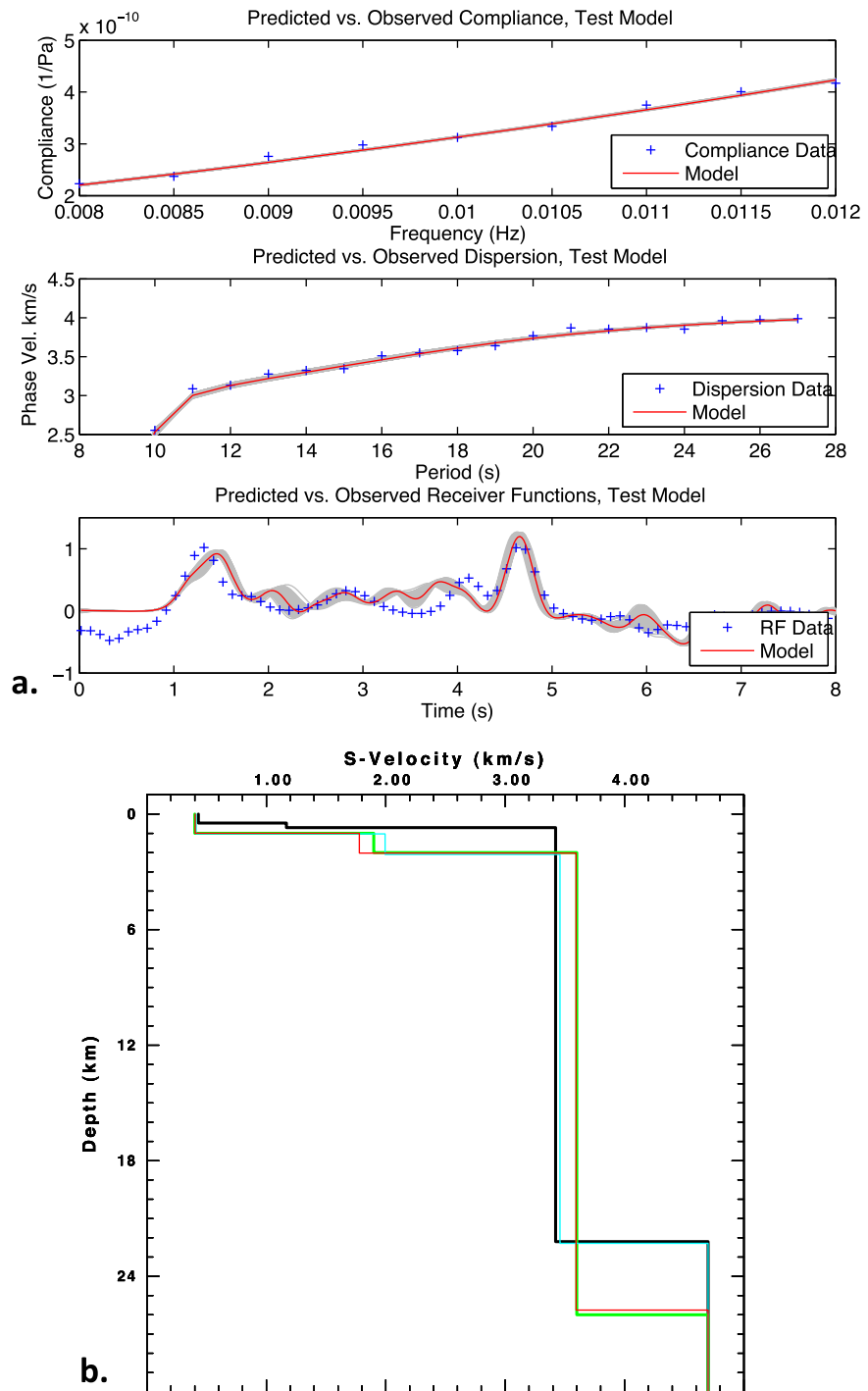
Figure 6. Synthetic recovery test. (a) Comparison of input and modeled compliance, surface wave, and receiver function data. (top) Observed versus predicted seafloor compliance data. (middle) Observed versus predicted surface-wave phase-velocity dispersion. (bottom) Observed versus predicted receiver functions. (b.) (green) Model used to generate synthetic compliance, receiver function, and surface wave dispersion data for synthetic recovery testing. (black) Starting model for Monte Carlo inversion (note that black model intentionally chosen to differ from green model used to generate synthetics). 10,000 random model realizations using bounds given in text were generated and tested. Resulting mean shear-velocity model from Monte Carlo inversion with receiver function SNR of 10 (red) recovers both sediment and crustal thickness, while receiver function with SNR of 5 (light blue) recovers only sediment thickness and does not deviate from the starting crustal thickness.

and correctly recovers sediment thickness to SNR as low as 5. In addition to this synthetic test, Monte Carlo results were compared to those of the Nelder-Mead Simplex nonlinear optimization method [*Lagarias et al.*, 1998] using a common starting model and found to agree well.
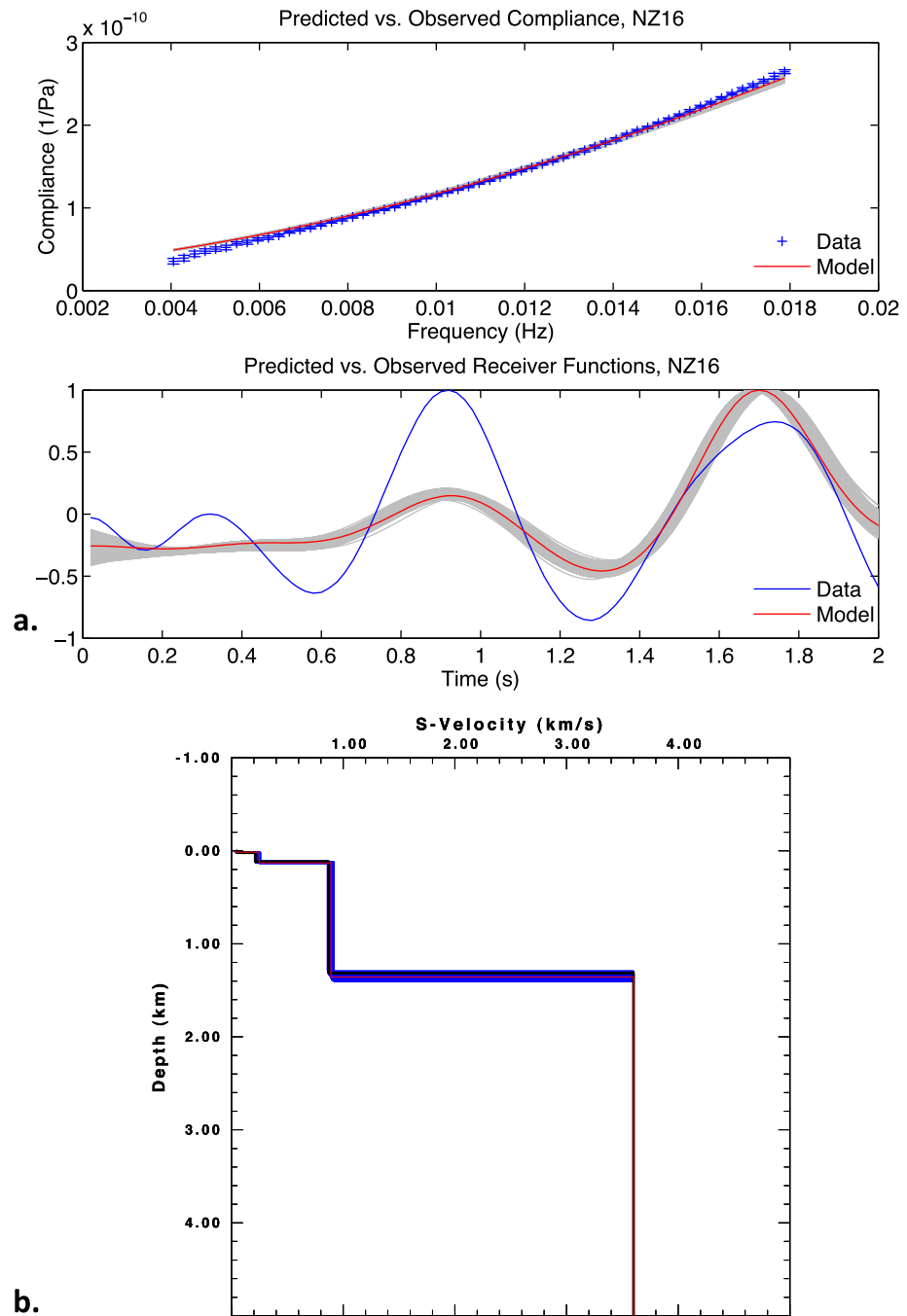
Figure 7. Joint compliance and receiver function inversion results for station NZ16 (surface waves not included—see Figure 10 for inversion including surface waves). The model was parameterized as three constant-velocity sediment layers. (a) Observed versus predicted seafloor compliance data (top) and receiver functions (bottom). (b) Starting (black) and mean posterior shear velocity model (red). Blue and gray-shaded regions indicate models and resulting data within one standard deviation of the posterior parameter means. Compliance and receiver function inversion results for station NZ16, parameterized as two sediment layers with linear velocity gradients. (c) Observed versus predicted seafloor compliance data (top) and receiver functions (bottom). (d.) Starting (black) and mean posterior shear velocity model (red). Blue and gray-shaded regions indicate models and data within one standard deviation of the posterior means.

4.2. Sediment Velocity Structure from P-S Mode Conversions and Seafloor Compliance at MOANA Stations

We jointly model MOANA seafloor compliance data and receiver functions using the MC algorithm to produce sediment velocity and thickness estimates for MOANA stations NZ06 and NZ16 (Figures 7 and 8). Only
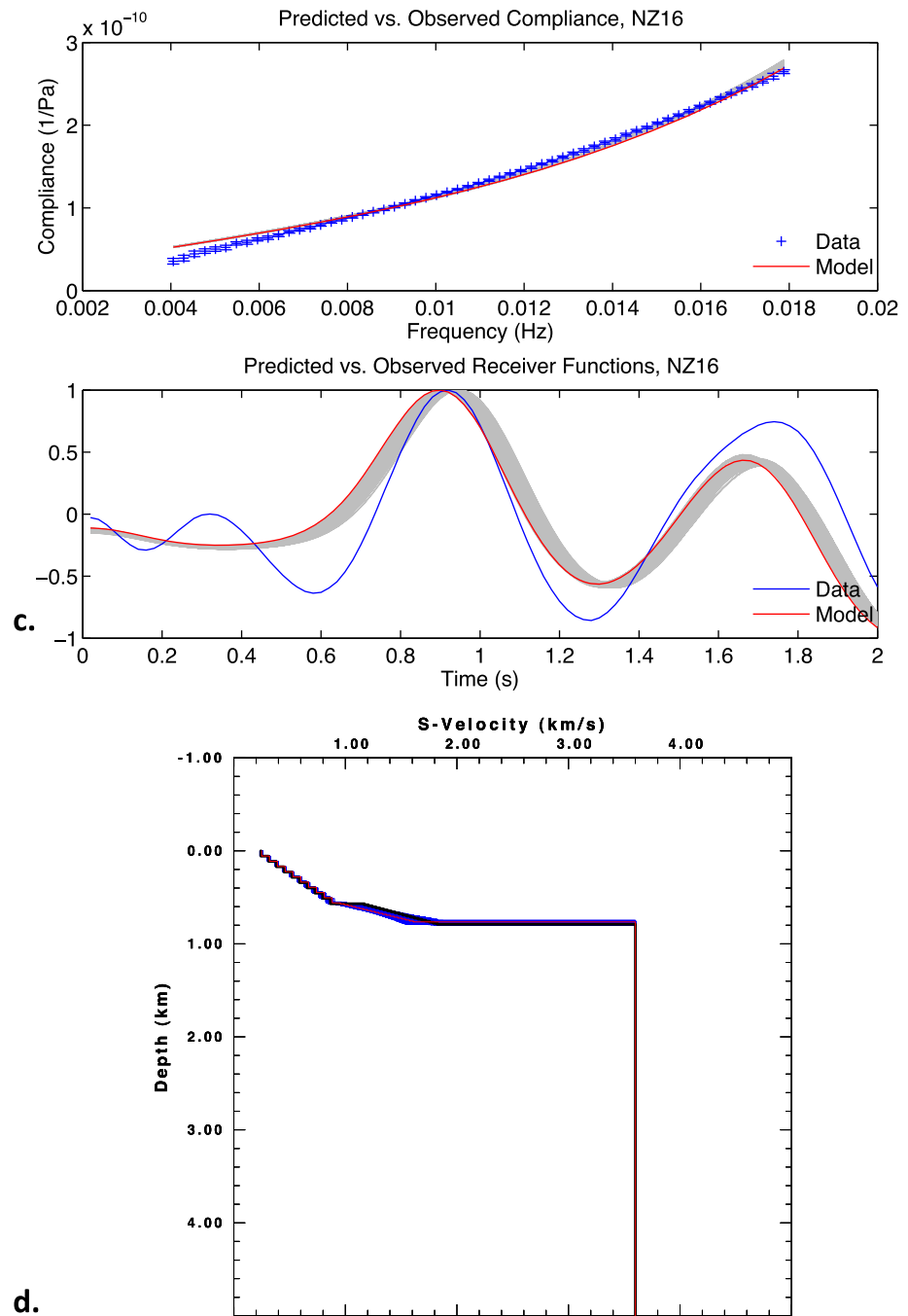
Figure 7. Continued.

the first 2 s of the receiver function waveforms are used in the sediment study in order to isolate the first sediment P-S conversions, which constrain only the total travel time through the sediment column. The sea-floor compliance data provide a complimentary constraint on sediment shear velocity.

To estimate sediment velocity structure, we fix crustal thickness in our model to the estimates of *Grobys et al.* [2008]. We then construct trial starting models with sediment thicknesses ranging between those presented in the sonobuoy/refraction results of *Divins* [2003] (assumed to be minimum thicknesses) and the gravity modeling results of *Wood and Woodward* [2002].

The Monte Carlo search was performed in successive stages of 5000 iterations with a burn-in period of 1000 iterations to allow Markov chain stabilization. Between stages, the misfit parameters were adjusted to
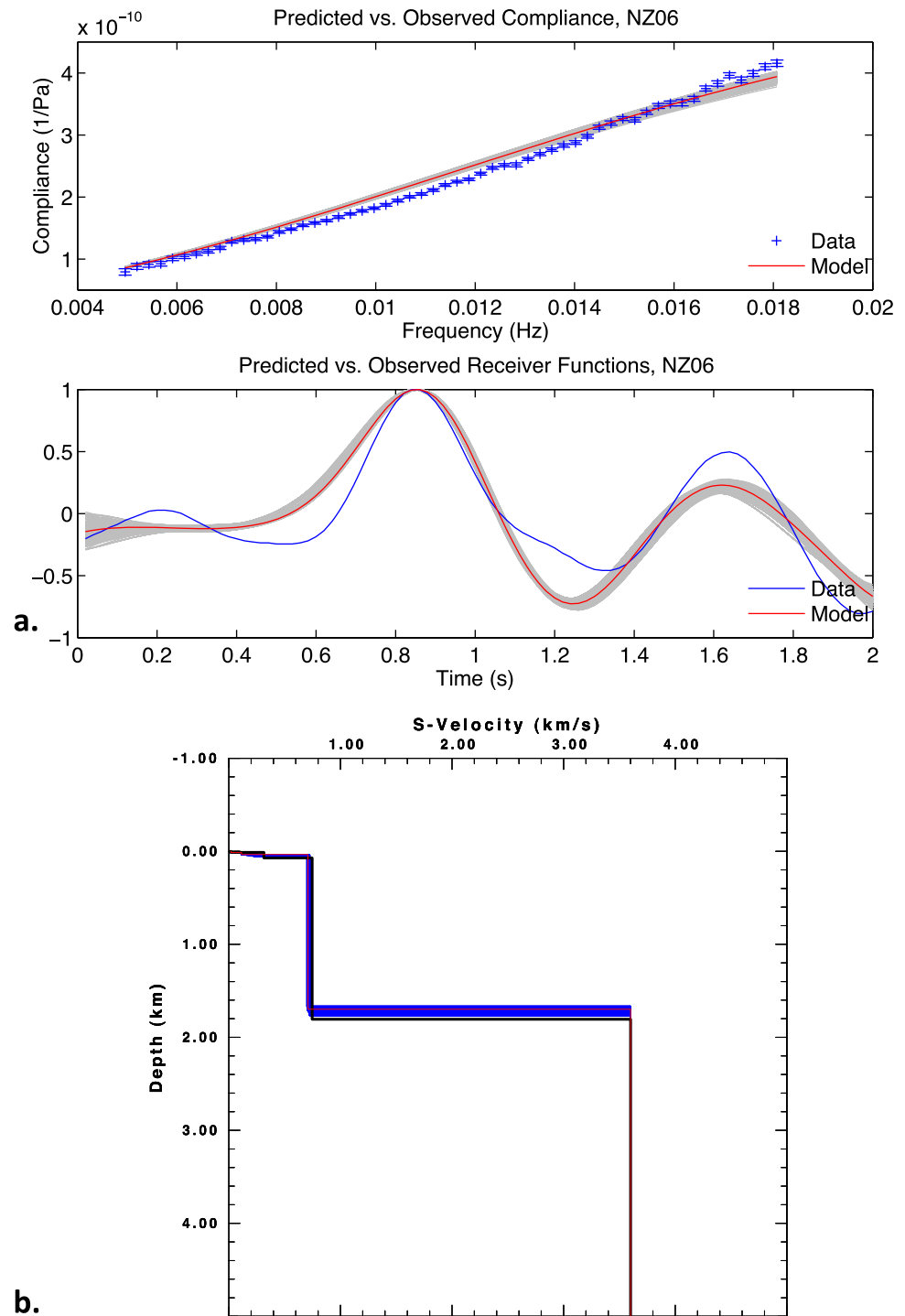
Figure 8. Compliance and receiver function inversion results for station NZ06, parameterized as three constant-velocity layers. (a) Observed versus predicted seafloor compliance data (top) and receiver functions (bottom). (b) Starting (black) and mean posterior shear velocity model (red). Blue and gray-shaded regions indicate models and data within one standard deviation of the posterior mean. Compliance and receiver function inversion results for station NZ06, parameterized as two sediment layers with linear velocity gradients. (c) Observed versus predicted seafloor compliance data (top) and receiver functions (bottom). (d) Starting (black) and mean posterior shear velocity model (red). Blue-shaded and gray-shaded regions indicate models and data within one standard deviation of the posterior mean.

weight receiver functions and seafloor compliance equally, and the starting model for the next stage was constructed using the posterior parameter Markov chain means from the previous stage. The resulting velocity models and data fits are presented here as the means of the parameter Markov chains ±1 standard
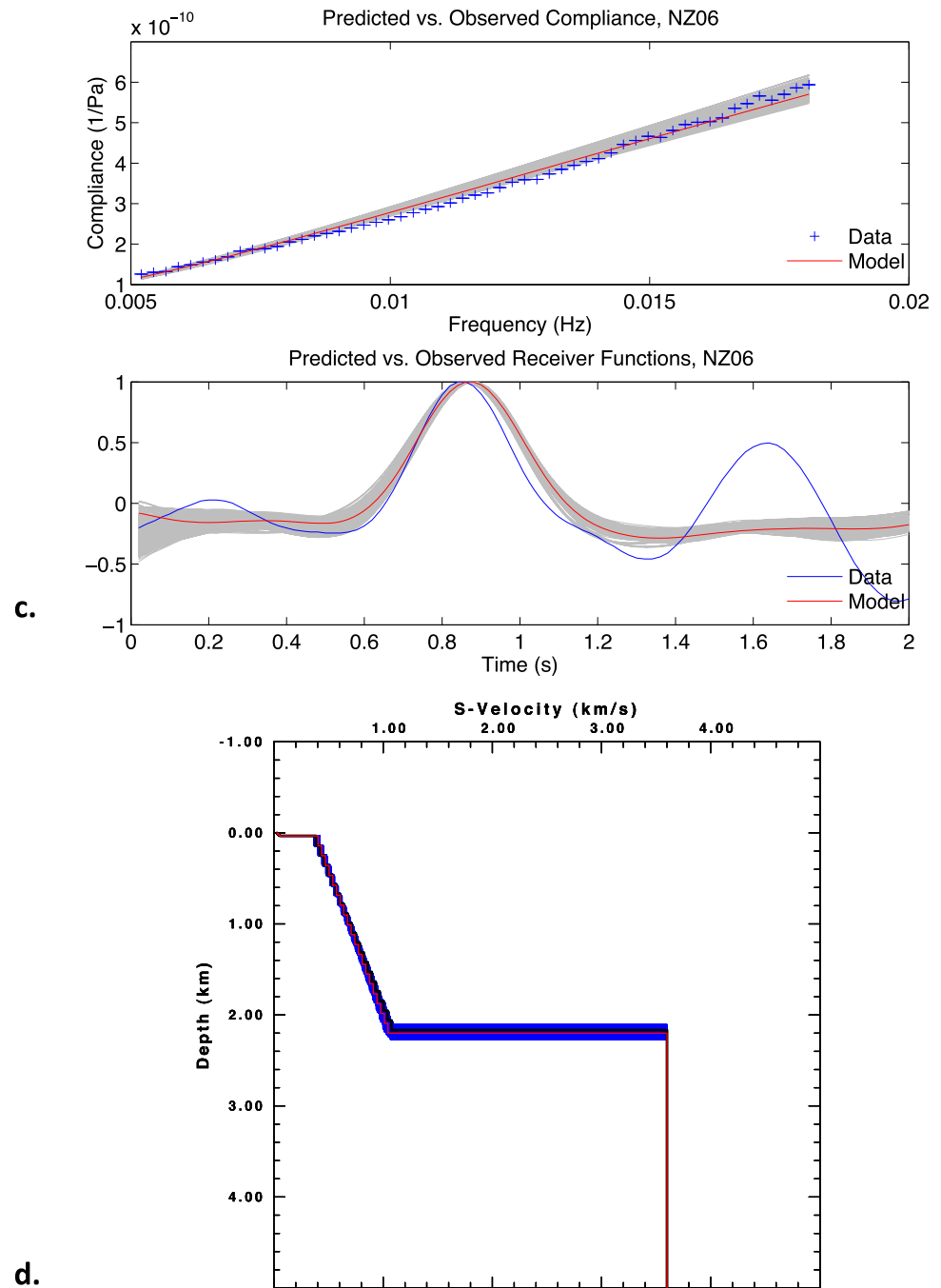
Figure 8. Continued.

deviation. The posterior parameter variances are not representative of true model uncertainties due to the absence of receiver function covariance estimates in this study.

4.2.1. Station NZ16

Station NZ16 is located on the Challenger Plateau, roughly 150 km off the west coast of the South Island and 200 km southeast of NZ06, at a water depth of 1063 m.

Receiver functions at NZ16 show a prominent double pulse in the first 2 s of the waveform that is coherent across the 30–90° epicentral distance bins (Figure 3a). This double pulse could result from multiple reverberations in a single sediment layer or indicate the presence of multiple impedance contrasts in the

sediment column. When searching over a model space of three constant-velocity layers, the Monte Carlo analysis of seafloor compliance and receiver functions predicts a total sediment thickness of 1.4 km but underpredicts the amplitude of the first receiver function pulse (Figure 7a). When linear velocity gradients are employed in the model, the receiver function fit improves markedly and the estimated sediment thickness decreases to only 800 m (Figures 7c and 7d).

4.2.2. Station NZ06
Station NZ06 is located ∼ 350 km off the west coast of the South Island of New Zealand on the Challenger Plateau in 859 m of water. Receiver functions at NZ06 show high-amplitude sediment reverberations and the waveforms are more weakly correlated across epicentral distance bins than those from NZ16 (Figure 3).

Monte Carlo results for the three-layered model at NZ06 estimate a total sediment thickness of 1.7 km, and indicate a shallow impedance contrast at 35m but fit the compliance curve poorly (Figure 8a). The linear-gradient model yields a total sediment thickness estimate of 2.2 km, exhibits no shallower discontinuities and does not fit the second pulse in the receiver function (Figures 8c and 8d).

4.3. Crustal Thickness and Shear Velocity Structure From Monte Carlo Modeling of Seafloor Compliance, Receiver Functions, and Rayleigh Dispersion
To investigate the feasibility of this technique in resolving deeper features such as the Moho, we added Rayleigh dispersion to the input data and extended the modeled receiver function waveforms to include arrivals originating from deeper structure. We use the means of the posterior model parameter distributions from the sediment analysis in subsection 4.2 combined with average crustal shear velocities from the surface-wave inversion in subsection 2.2.1 to form starting models for the crustal-scale analysis (Figure 9). Starting Moho depths were estimated using *Grobys et al.* [2008]. Misfit in the predicted versus observed receiver functions is calculated to 6 s in the waveform to include Moho P-S conversions and reverberations. Predicted versus observed phase velocity dispersion is added to the misfit functional and the algorithm is run in the same manner as discussed in subsection 4.2 above. Due to low SNR in the MOANA receiver functions, the full crustal-scale combined receiver function, surface wave, and compliance analysis is limited to station NZ16.

A total crustal thickness of 22 km is obtained from joint inversion of RFs, compliance, and surface wave data at NZ16 (Figure 9). However, in the starting model, a Moho depth of 22 km was used based on the models of *Grobys et al.* [2008], and the Monte Carlo accepted no model realizations that deviated substantially from this value, as shown by the posterior crustal thickness standard deviation plotted in blue shading in Figure 9b. Our synthetic test showed similar behavior at receiver function SNR below 10 (Figure 6) illustrating that receiver function data sensitivity is poor at longer times in the waveform due to noise, and that a local minimum in the cost function around the starting crustal thickness could result from using noisy receiver functions in this method. The shallow sediment parameters were left free in the deeper inversion and a sediment layer thickness of 800 m was estimated, falling near the values of 711 m and 800 m produced by the constant-velocity and linear gradient sediment-scale analysis (Figure 7).

5. Discussion
At station NZ16 the estimated sediment thickness of 800 m from the gradient model agrees generally with the 711 m acoustic basement depth reported by *Divins* [2003]. Sediment thickness estimates from both the three layer and gradient models fall within the 2.0 ± 1.5km thickness estimate from gravity modeling by *Wood and Woodward* [2002], but the gradient model yields lower joint misfit at this station. We also observe shear resonances in horizontal-component ambient noise data at NZ16 that are potentially related to the presence of shear velocity gradients in the shallow sediments there [*Godin and Chapman*, 1999].

When the surface wave data are modeled in conjunction with receiver functions at NZ16, we estimate a crustal thickness of 22 km, which does not deviate from the 22 km starting Moho depth we assume from *Grobys et al.* [2008]. The implausibly low standard deviation of the posterior crustal thickness illustrates that the joint misfit is not being substantially reduced by varying this parameter in the Monte Carlo search. This behavior was also seen in our synthetic testing (Figure 6). According to our synthetic tests, a receiver function SNR on the order of 10 is likely necessary to constrain crustal thickness with this method. This is
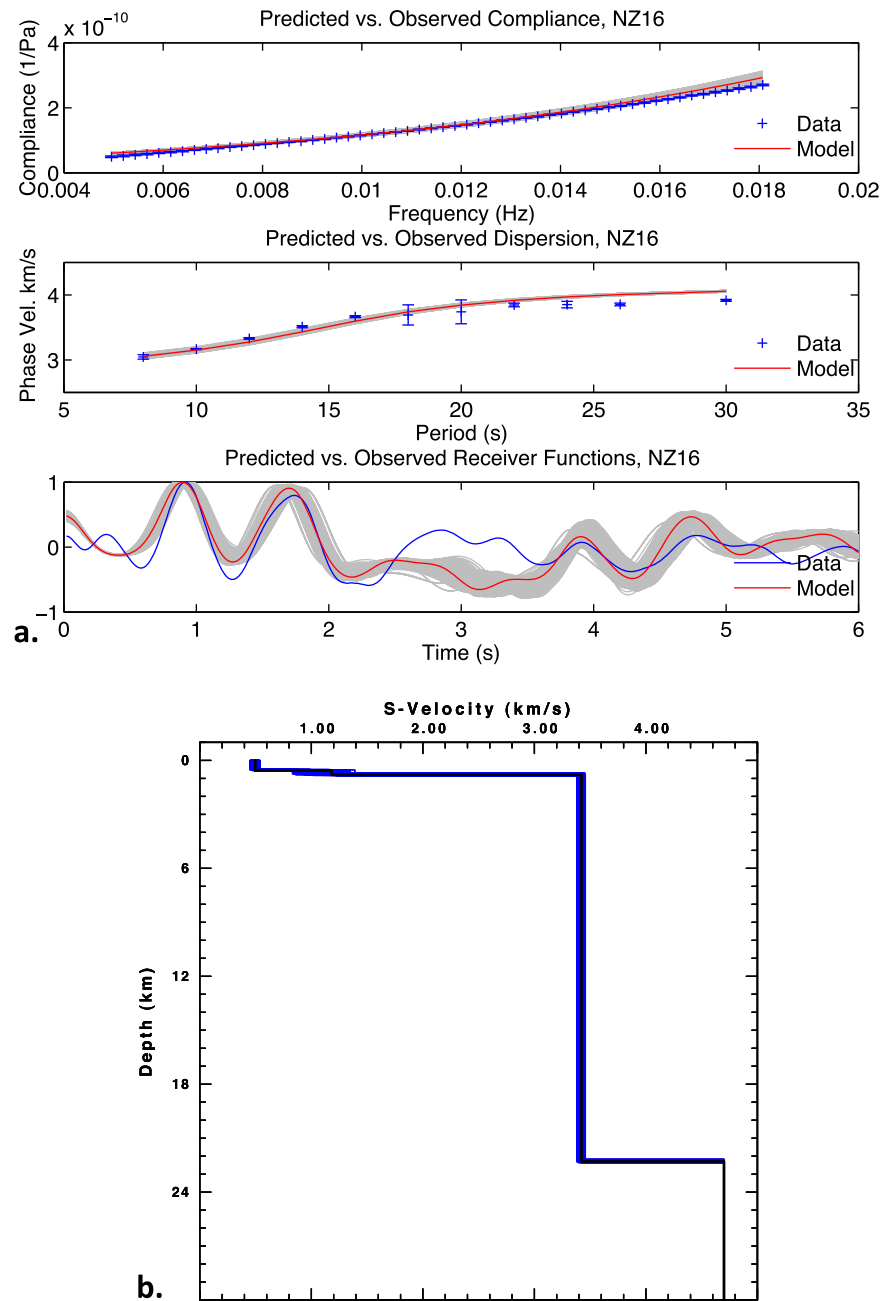
Figure 9. (a) Joint inversion of Rayleigh phase velocities, seafloor compliance, and receiver functions at station NZ16. (b) Inversion results at NZ16. Our mean model (red) crustal thickness of 22km does not deviate from our starting estimate (black) because noise in the receiver function at later times prevents it from constraining crustal thickness in the inversion.

atypically high for events used in this study. For instance, at station NZ16 only six radial receiver functions had SNR > 3. Thus, based on these results, we cannot robustly constrain interface depths below the sediment-basement contact.

At station NZ06, our three-layered model predicts a total sediment thickness of 1.7 km, within the bounds of 2.5 ± 1.5 km estimated by *Wood and Woodward* [2002]. A large shallower discontinuity is predicted at 35 m, and the model produces no interface corresponding with the 466 m depth to acoustic basement reported by *Divins* [2003]. The 2.2 km sediment thickness resulting from the gradient model at NZ06 also falls within the range reported by *Wood and Woodward* [2002], but produces poorer fits to the receiver function data than the three-layered model. The horizontal-component resonances that we observe at

NZ16 and associate with the presence of shallow sediment shear velocity gradients are not prominently seen on NZ06 noise data.

It is evident from these results that the choice of model parameterization has a crucial influence on sediment models resulting from the inversion of seafloor compliance and receiver function data. Based on joint data misfit, the linear-gradient model is more appropriate for NZ16, while the layer-cake model is preferred at NZ06. Our observations of sediment shear modes also support the presence of large shallow velocity gradients at NZ16 but not at NZ06.

Seafloor compliance probes bulk shear velocities while receiver functions are sensitive to impedance contrasts across interfaces. We find that the simple parameterizations investigated here are not always sufficient to jointly model features demanded by these separate datasets. For example, the compliance data for NZ06 are best fit by a linear velocity gradient, but this parameterization does not result in a model with the dual impedance contrasts required to fit both receiver function pulses. A nonlinear velocity gradient parameterized using a power law [*Godin and Chapman*, 1999] or spline [*Shen et al*., 2013] formulation may provide an improved fit to the slope of the compliance curve while allowing for the large impedance contrasts necessary to fit the receiver function data.

The evident trade-off in data sensitivity between compliance and receiver functions also motivates the use of a transdimensional inversion scheme for these data, in which the model parameterization itself is treated as an unknown [*Bodin et al*., 2012]. In addition, data noise can be treated as a free parameter in a transdimensional Monte Carlo search. In such case, the posterior distributions would reflect meaningful model uncertainties, rather than simply depending on ad hoc cost-function weighting parameters as they do in this study.

Our receiver function data did not conclusively resolve crustal structure beneath the sediment layer with this method. However, an alternate technique to mitigate the overprinting effects of sediments in OBS receiver functions is redatuming to virtual receivers below the sediments, as successfully applied on land data from the Mississippi Embayment by *Langston* [2011]. The success of redatuming relies critically upon accurate a priori knowledge of sediment thickness and velocity structure. Promisingly, the method we present here can be used to estimate these parameters using P-S converted arrival times and seafloor compliance data to, respectively, constrain sediment thickness and shear velocity, opening up a potential research avenue for improving the utility of OBS receiver functions in the future.

6. Conclusions

We introduce a new method to combine seafloor compliance, receiver functions, and Rayleigh wave dispersion in order to determine suboceanic crustal properties. We utilize a Markov Chain Monte Carlo approach to sample the model space and produce probabilistic estimates of shear velocity structure. We use the method to first determine shallow sediment properties, which are then used as an a priori estimate in our modeling of the deeper crust. Well-determined sediment properties are essential for modeling the sediment layer reverberations that can dominate OBS receiver functions. Our tests with synthetic data are promising. However, tests with real data are mixed. We have good success in determining shallow sediment properties from the combination of seafloor compliance and receiver functions, and good success in determining crustal shear wave velocity from the combination of seafloor compliance and Rayleigh wave dispersion. Our results with synthetic and real data indicate that resolution of the Moho interface from OBS receiver functions remains elusive, even in combination with a well-determined sedimentary layer. Redatuming methods may hold more promise, and will rely on a well-determined sedimentary layer, as provided here. Our success in determining shallow interface properties suggests that our method may be of use for application to other shallow targets, such as magma chambers or hydrocarbon reservoirs.

References

Bodin, T., M. Sambridge, H. Tkalčić, P. Arroucau, K. Gallagher, and N. Rawlinson (2012), Transdimensional inversion of receiver functions and surface wave dispersion, *J. Geophys. Res.*, *117*, B02301, doi:10.1029/2011JB008560.
Bostock, M. G., and A. M. Trehu (2012), Wave-field decomposition of ocean bottom seismograms, *Bull. Seismol. Soc. Am.*, *102*, 1681–1692.
Castagna, J. P., M. L. Batzle, and R. L. Eastwood (1985), Relationships between compressional-wave and shear-wave velocities in clastic silicate rocks, *Geophysics*, *50*(4), 571–581.

Collins, J. A., and P. Molnar (2014), Pn anisotropy beneath the South Island of New Zealand and implications for distributed deformation in continental lithosphere, *J. Geophys. Res. Solid Earth*, *119*, doi:10.1002/2014JB011233.

Crawford, W., S. C. Webb, and J. Hildebrand (1991), Seafloor compliance observed by long-period pressure and displacement measurements, *J. Geophys. Res.*, *96*(10), 16,151–16,160.

Divins, D. L. (2003), *Total Sediment Thickness of the World's Oceans & Marginal Seas*, NOAA Natl. Geophys. Data Cent., Boulder, Colo.

Filloux, J. H. (1983), Pressure fluctuations on the open ocean floor off the Gulf of California: Tides, Earthquakes, Tsunamis, *J. Phys. Oceanogr.*, *13*, 783–786.

Forsyth, D. W., S. C. Webb, L. M. Dorman, and Y. Shen (1998), Phase velocities of Rayleigh waves in the MELT experiment on the East Pacific Rise, *Science*, *280*, 1235–1238, doi:10.1126/science.280.5367.1235.

Godin, O. A., and D. M. F. Chapman (1999), Shear-speed gradients and ocean seismo-acoustic noise resonances, *J. Acoust. Soc. Am.*, *106*(5), 2367–2381.

Grobys, J. W. G., K. Gohl, and G. Eagles (2008), Quantitative tectonic reconstructions of Zealandia based on crustal thickness estimates, *Geochem. Geophys. Geosyst.*, *9*, Q01005, doi:10.1029/2007GC001691.

Haario, H., M. Laine, A. Mira, and E. Saksman (2006), DRAM: Efficient adaptive MCMC, *Stat. Comput.*, *16*, 339–354, doi:10.1007/s11222-006-9438-0.

Harmon, N., D. W. Forsyth, R. Lamm, and S. C. Webb (2007), P and S wave delays beneath intraplate volcanic ridges and gravity lineations near the East Pacific Rise, *J. Geophys. Res.*, *112*, B03309, doi:10.1029/2006JB004392.

Herrmann, R. B. (2013), Computer programs in seismology: An evolving tool for instruction and research, *Seismo. Res. Lett.*, *84*, 1081–1088, doi:10.1785/0220110096.

Herrmann, R. B., and C. J. Ammon (2004), Surface waves, receiver functions and crustal structure, in *Computer Programs in Seismology*, version 3.30, St. Louis Univ., Saint Louis, Mo.

Hetényi, G., R. Cattin, J. Vergne, and J. L. Nábělek (2006), The effective elastic thickness of the India plate from receiver function imaging, gravity anomalies and thermomechanical modeling, *Geophys. J. Int.*, *167*(3), 1106–1118.

Kennett, J. P., et al. (1975), Site 284, in *Initial Reports of the Deep Sea Drilling Project*, vol. 29, edited by J. P. Kennett et al., pp. 403–445, U.S. Gov. Print. Off., Washington, D. C., doi:10.2973/dsdp.proc.29.111.1975.

Lagarias, J. C., J. A. Reeds, M. H. Wright, and P. E. Wright (1998), Convergence properties of the Nelder-Mead simplex method in low dimensions, *SIAM J. Optim.*, *9*(1), 112–147.

Langston, C. (1979), Structure under Mount Rainier, Washington, inferred from teleseismic body waves, *J. Geophys. Res.*, *84*(B9), 4749–4762.

Langston, C. (2011), Wave-field continuation and decomposition for passive seismic imaging under deep unconsolidated sediments, *Bull. Seismol. Soc. Am.*, *101*(5), 2176–2190.

Leahy, G. M., J. A. Collins, C. J. Wolfe, G. Laske, and S. C. Solomon (2010), Underplating of the Hawaiian swell: Evidence from teleseismic receiver functions, *Geophys. J. Int.*, *183*(1), 313–329.

Ligorria, J., and C. Ammon (1999), Iterative deconvolution and receiver-function estimation, *Bull. Seismol. Soc. Am.*, *89*(5), 1395–1400.

Lin, F.-C., M. H. Ritzwoller, J. Townend, S. Bannister, and M. K. Savage (2007), Ambient noise Rayleigh wave tomography of New Zealand, *Geophys. J. Int.*, *170*(2), 649–666.

Lin, F.-C., M. P. Moschetti, and M. H. Ritzwoller (2008), Surface wave tomography of the western United States from ambient seismic noise: Rayleigh and Love wave phase velocity maps, *Geophys. J. Int.*, *173*, 281–298, doi:10.1111/j.1365-246X.2008.03720.x.

Lin, F.-C., M. H. Ritzwoller, and R. Snieder (2009), Eikonal Tomography: Surface wave tomography by phase-front tracking across a regional broad-band seismic array, *Geophys. J. Int.*, *177*, 1091–1110, doi:10.1111/j.1365-246X.2009.04105.x.

Mosegaard, K., and A. Tarantola (1995), Monte Carlo sampling of solutions to inverse problems, *J. Geophys. Res.*, *100*(B7), 12,431–12,447.

Owens, T. J., G. Zandt, and S. R. Taylor (1988), Seismic evidence for an ancient rift beneath the Cumberland Plateau, Tennessee: A detailed analysis of broadband teleseismic P waveforms, *Bull. Seismol. Soc. Am.*, *78*, 96–108.

Park, J., and V. Levin (2000), Receiver functions from multiple-taper spectral correlation estimates, *Bull. Seismol. Soc. Am.*, *90*(6), 1507–1520.

Ritzwoller, M. H., and A. L. Levshin (2002), Estimating shallow shear velocities with marine multicomponent seismic data, *Geophysics*, *67*(6), 1991–2004.

Scherwath, M., T. Stern, F. Davey, D. Okaya, W. S. Holbrook, R. Davies, and S. Kleffmann (2003), Lithospheric structure across oblique continental collision in New Zealand from wide-angle P wave modeling, *J. Geophys. Res.*, *108*(B12), 2566, doi:10.1029/2002JB002286.

Shen, W., M. H. Ritzwoller, V. Schulte-Pelkum, and F.-C. Lin (2013), Joint inversion of surface wave dispersion and receiver functions: A Bayesian Monte-Carlo approach, *Geophys. J. Int.*, *192*, 807–836, doi:10.1093/gji/ggs050.

Stachnik, J. C., K. Dueker, D. L. Schutt, and H. Yuan (2008), Imaging Yellowstone plume-lithosphere interactions from inversion of ballistic and diffusive Rayleigh wave dispersion and crustal thickness data, *Geochem. Geophys. Geosyst.*, *9*, Q06004, doi:10.1029/2008GC001992.

Stern, T., D. Okaya, and M. Scherwath (2002), Structure and strength of a continental transform from onshore-offshore seismic profiling of South Island, New Zealand, *Earth Planet. Space*, *54*(11), 1011–1020.

Thorwart, M., and T. Dahm (2005), Wavefield decomposition for passive ocean bottom seismological data, *Geophys. J. Int.*, *163*(2), 611–621.

Van Avendonk, H., J. A., W. S. Holbrook, D. Okaya, J. K. Austin, F. Davey, and T. Stern (2004), Continental crust under compression: A seismic refraction study of South Island Geophysical Transect I, South Island, New Zealand, *J. Geophys. Res.*, *109*, B06302, doi:10.1029/2003JB002790.

Webb, S. C. (1998), Broadband seismology and noise under the ocean, *Rev. Geophys.*, *36*(1), 105–142.

Willoughby, E., and R. Edwards (2000), Shear velocities in Cascadia from seafloor compliance, *Geophys. Res. Lett.*, *27*(7), 1021–1024.

Wood, R., and D. Woodward (2002), Sediment thickness and crustal structure of offshore Western New Zealand from 3d gravity modeling, *N. Z. J. Geol. Geophys.*, *45*(2), 243–255.

Yang, Z., A. F. Sheehan, J. A. Collins, and G. Laske (2012), The character of seafloor ambient noise recorded offshore New Zealand: Results from the MOANA ocean bottom seismic experiment, *Geochem. Geophys. Geosyst.*, *13*, Q10011, doi:10.1029/2012GC004201.

Ye, T., W. Shen, and M. H. Ritzwoller (2013), Crustal and uppermost mantle shear velocity structure adjacent to the Juan de Fuca Ridge from ambient seismic noise, *Geochem. Geophys. Geosyst.*, *14*, 3221–3233, doi:10.1002/ggge.20206.

Zietlow, D. W., A. F. Sheehan, P. H. Molnar, M. K. Savage, G. Hirth, J. A. Collins, and B. H. Hager (2014), Upper mantle seismic anisotropy at a strike slip boundary: South Island, New Zealand, *J. Geophys. Res. Solid Earth*, *119*, 1020–1040, doi:10.1002/2013JB010676.